IJMMM
International Journal of
Minerals, Metallurgy and Materials
矿物冶金与材料学报（英文版）

Characterization and ultraviolet–visible shielding property of samarium–cerium compounds containing Sm_2O_2S prepared by co-precipitation method

Yanping Li, Xue Bian, Xun Jin, Peng Cen, Wenyuan Wu, and Gaofeng Fu

Cite this article as:

Yanping Li, Xue Bian, Xun Jin, Peng Cen, Wenyuan Wu, and Gaofeng Fu, Characterization and ultraviolet–visible shielding property of samarium–cerium compounds containing Sm_2O_2S prepared by co-precipitation method, *Int. J. Miner. Metall. Mater.*, 29(2022), No. 9, pp. 1809-1816. https://doi.org/10.1007/s12613-021-2309-z

View the article online at SpringerLink or IJMMM Webpage.

Articles you may be interested in

J. Celina Selvakumari, M. Ahila, M. Malligavathy, and D. Pathinettam Padiyan, Structural, morphological, and optical properties of tin(IV) oxide nanoparticles synthesized using *Camellia sinensis* extract:a green approach, *Int. J. Miner. Metall. Mater.*, 24(2017), No. 9, pp. 1043-1051. https://doi.org/10.1007/s12613-017-1494-2

Rui-qi Yang, Na Liang, Xuan-yu Chen, Long-wei Wang, Guo-xin Song, Yan-chen Ji, Na Ren, Ya-wei Lü, Jian Zhang, and Xin Yu, Sn/Sn_3O_{4-x} heterostructure rich in oxygen vacancies with enhanced visible light photocatalytic oxidation performance, *Int. J. Miner. Metall. Mater.*, 28(2021), No. 1, pp. 150-159. https://doi.org/10.1007/s12613-020-2131-z

Hassan Esmaili, Amir Kotobi, Saeed Sheibani, and Fereshteh Rashchi, Photocatalytic degradation of methylene blue by nanostructured Fe/FeS powder under visible light, *Int. J. Miner. Metall. Mater.*, 25(2018), No. 2, pp. 244-252. https://doi.org/10.1007/s12613-018-1567-x

Betül Kafkaslıolu Yıldız, Hüseyin Yılmaz, and Yahya Kemal Tür, Influence of nickel addition on the microstructure and mechanical properties of Al_2O_3-5vol%ZrO_2 ceramic composites prepared via precipitation method, *Int. J. Miner. Metall. Mater.*, 26(2019), No. 7, pp. 908-914. https://doi.org/10.1007/s12613-019-1792-y

Zhu Wang, Lei Zhang, Xian Tang, Zhao-yang Cui, Jun-peng Xue, and Min-xu Lu, Investigation of the deterioration of passive films in H_2S-containing solutions, *Int. J. Miner. Metall. Mater.*, 24(2017), No. 8, pp. 943-953. https://doi.org/10.1007/s12613-017-1482-6

Long Meng, Zhan-cheng Guo, Jing-kui Qu, Tao Qi, Qiang Guo, Gui-hua Hou, Peng-yu Dong, and Xin-guo Xi, Synthesis and characterization of Co_3O_4 prepared from atmospheric pressure acid leach liquors of nickel laterite ores, *Int. J. Miner. Metall. Mater.*, 25(2018), No. 1, pp. 20-27. https://doi.org/10.1007/s12613-018-1542-6

IJMMM WeChat

QQ author group

International Journal of Minerals, Metallurgy and Materials
Volume 29, Number 9, September 2022, Page 1809
https://doi.org/10.1007/s12613-021-2309-z

Characterization and ultraviolet–visible shielding property of samarium–cerium compounds containing Sm_2O_2S prepared by co-precipitation method

Yanping Li[1,2], *Xue Bian*[1,2],✉, *Xun Jin*[1,2], *Peng Cen*[1,2], *Wenyuan Wu*[1,2], *and Gaofeng Fu*[1,2]

1) Key Laboratory of Ecological Metallurgy of Multi-metal Intergrown Ores of Ministry of Education, Shenyang 110819, China
2) School of Metallurgy, Northeastern University, Shenyang 110819, China

(Received: 29 March 2021; revised: 24 May 2021; accepted: 27 May 2021)

Abstract: Since ultraviolet (UV) light, as well as blue light, which is part of visible light, is harmful to skin, samarium–cerium compounds containing Sm_2O_2S were synthesized by co-precipitation method. This kind of compounds blocks not only UV light, but also blue light. The minimum values of average transmittance (360–450 nm) and band gap of samarium–cerium compounds were 8.90% and 2.76 eV, respectively, which were less than 13.96% and 3.01 eV of CeO_2. Elemental analysis (EA), X-ray diffraction (XRD), Fourier transformation infrared (FTIR), and Raman spectra determined that the samples contained Ce_4O_7, Sm_2O_2S, Sm_2O_3, and $Sm_2O_2SO_4$. The microstructure of samples was analyzed by scanning and transmission electron microscopies (SEM and TEM). X-ray photoelectron spectrum (XPS) showed that cerium had Ce^{3+} and Ce^{4+} valence states, and oxygen was divided into lattice oxygen and oxygen vacancy, which was the direct cause of the decrease of average transmittance and band gap.

Keywords: band gap; co-precipitation method; samarium–cerium compound; ultraviolet light; blue light

1. Introduction

Ultraviolet (UV) light is always divided into UVA (320–400 nm), UVB (280–320 nm), and UVC (200–280 nm). Among them, the UVA has the strongest carcinogenicity and thus becomes the main inducement of skin wrinkle, ageing, flabby, and dark spot. To reduce the damage of UV light to human body, a large number of UV-shielding materials have been developed, and they can generally be split in two categories: organic absorbent and inorganic blocker. The organic matters used to absorb the UV usually decompose easily. The toxicity and skin irritation also limit its wide application. By contrast, the inorganic blockers have better advantages due to its stability and non-toxic. At present, the inorganic blockers mainly include titanium dioxide (TiO_2) [1], zinc oxide (ZnO) [2], and cerium dioxide (CeO_2) [3–4]. Among them, CeO_2 has a competitive advantage over the others in UV-shielding [5–7]. This is mainly attributed to the variable valences of cerium. The presence of Ce^{3+} leads to the formation of oxygen vacancy that produces a donor level at the bottom of the conduction band. However, CeO_2 has no good shielding effect on UVA.

In addition to the UV, blue light, which has the shortest wavelength (400–450 nm) in the visible spectrum, will also cause hyperpigmentation and accelerate skin relaxation and aging [8]. A variety of blue light absorbers, mainly including Al_2O_3/polyacrylic acid mixture, TiO_2/polyacrylic acid mixture [9–10], Fe_2O_3/polyacrylic acid mixture, metal complex dyes, benzotriazole compounds [11], PMMA methyl acrylic acid, and fullerenes [12], have been proposed. Nevertheless, to the best of our knowledge, the composites that can shield both ultraviolet and blue light have never been previously reported.

Rare-earth oxysulfides have high light absorption and energy transfer efficiency, making them an important class of optical functional materials [13]. Sm_2O_2S in rare-earth oxysulfides can also be used as a laser stealth absorbent due to its transition from ground state $6H_{5/2}$ to excited state $6F_{9/2}$ of Sm^{3+} [14]. Considering this, a mixture of cerium oxide and Sm_2O_2S may extend the shielding range of single CeO_2 to the blue light. For the moment, there is no report on the preparation method of the mixture of cerium oxide and Sm_2O_2S. Therefore, the preparation methods of cerium oxide and rare-earth oxysulfides were introduced respectively, and then a compromise method will be selected for sample preparation.

The methods of synthesizing cerium dioxide mainly include precipitation method [15–16], sol–gel method [17], sonochemistry method [18–19], electrochemical synthesis method [20], and hydrothermal method [21–27]. Flux fusion is the most commonly used method to synthesize rare earth oxysulfides as well as other complex oxysulfides [28–34]. The crystal development of the samples prepared by flux fusion method is complete and the crystal properties are good. However, the process is always operated at a high temperat-

---

✉ Corresponding author: Xue Bian E-mail: bianx@smm.neu.edu.cn

ure for a long time, and thus it is difficult to effectively control the reaction. There are some other methods, such as thermal decomposition method [35–36], solid–gas synthesis [37], hydrothermal method [38], homogeneous precipitation method [39–40], radio-frequency sputtering [41], sol–gel polymer thermolysis method [42], and vapor phase growth [43].

In this paper, we tried to synthesize the compounds of cerium oxide and Sm_2O_2S by co-precipitation method. The advantages of this method are simple operation and low energy consumption. The material prepared by co-precipitation method had good UV–visible shielding performance. The impacts of pH value on the element content, phase composition, apparent morphology, surface element content, average transmittance (360–450 nm), and band gap were analyzed in detail.

2. Experimental

2.1. Materials

Cerium nitrate hexahydrate ($Ce(NO_3)_3{\cdot}6H_2O$) and samarium nitrate hexahydrate ($Sm(NO_3)_3{\cdot}6H_2O$) were employed as cerium source and samarium source, respectively. Sodium thiosulfate pentahydrate ($Na_2S_2O_3{\cdot}5H_2O$) played a role of precipitant. Polyvinyl pyrrolidone (PVP) was a dispersant agent. Sodium hydroxide (NaOH) was used to adjust pH. All these chemicals used were of analytical grade and used as received without further purification.

2.2. Synthesis

43.412 g $Ce(NO_3)_3{\cdot}6H_2O$ and 133.338 g $Sm(NO_3)_3{\cdot}6H_2O$ were mixed in water system, and then 10 g PVP and 99.272 g $Na_2S_2O_3{\cdot}5H_2O$ were added to the mixed solution successively. The pH value was adjusted to 8, 10, and 12 with NaOH precursors (6 mol/L), and the reaction was performed at 50°C for 3 h at a constant stirring rate of 800 r/min. After the reaction, the mixed solution was filtered, and the precipitation was washed thrice with water and with ethanol for another three times. The dried precursors were roasted in a tube furnace with high pure nitrogen flow in 500°C for 3 h to obtain three groups of samples.

2.3. Materials characterization

Ion concentrations were measured by an ICS-1100 ion chromatograph. Elemental analysis (EA) was performed on a Vario EL cube elemental analyzer. X-ray diffraction (XRD) analysis of samples was carried out on a Bruker AXS D8 Advance X-ray diffractometer with Cu K_α radiation (λ = 0.15406 nm). The scanning rate was 1°/min in the 2θ range from 20° to 70°. Fourier transformation infrared (FTIR) was performed on Bruker Vertex 70. Renishaw inVia Raman microscopy was used to obtain Raman spectrum. Scanning electron microscopy (SEM, voltage 20 kV) was performed on ULTRA PLUS instrument and transmission electron microscopy (TEM) measurements were performed using a Tecnai G2 F20 S-TWIN field-emission transmission electron microscope. X-ray photoelectron spectrum (XPS) measurement was performed on a Thermo escalab 250Xi spectrometer. UV–visible (UV–Vis) transmittance curves were observed under ambient condition on a UV-2550 spectrophotometer (Shimazu Company, Japan) equipped with an integrating sphere in the wavelength between 200 and 800 nm.

2.4. Calculation of band gap

The Tauc plot method [44–45] was used to obtain band gap. The formula is as shown in Eq. (1).

$$(\alpha hv)^{1/n} = A\left(hv - E_g\right) \tag{1}$$

where α is light absorption index; A is a constant related to energy; h is Planck constant; v is frequency; E_g is band gap of the semiconductor; n is related to the type of semiconductor, as the prepared samples are direct semiconductors, n is substituted into 0.5.

3. Results and discussion

Sodium thiosulfate solution may include $S_2O_3^{2-}$, S^{2-}, SO_4^{2-}, and SO_3^{2-}. In order to verify the existence state of sulfur element in the reaction system, the contents of SO_4^{2-} and SO_3^{2-} in sodium thiosulfate solution under different pH were tested, and the results are listed in Table 1. The concentration of SO_4^{2-} and SO_3^{2-} is determined by ion chromatography. S^{2-} is deduced from the conservation of charge. With the increase in pH, the content of SO_4^{2-} in the solution is gradually increasing, whereas that of SO_3^{2-} was always less than 10^{-6} g/L. Therefore, the solution mainly contained $S_2O_3^{2-}$, SO_4^{2-}, and S^{2-}. S^{2-} and SO_4^{2-} are obtained by the decomposition of $S_2O_3^{2-}$ according to the conservation of charge, so the change trend of S^{2-} with pH should be consistent with SO_4^{2-}. The titration curve was used to further determine the reaction process (Fig. 1). When pH value is less than 10, with the addition of NaOH, the curve is steep. At this time, part of the precipitation generated is samarium/cerium hydroxide, and the other part is formed by the complex of $S_2O_3^{2-}/S^{2-}$ and samarium (The reason for the absence of cerium will be explained in subsequent tests). With the further increase in pH, the slope of the curve slows down, indicating that the added NaOH is consumed in large quantities, so a large number of samarium/

Table 1. Concentration and proportion of SO_4^{2-}, SO_3^{2-}, S^{2-}, and $S_2O_3^{2-}$ in sodium thiosulfate solution

Sample	Ion concentration / (g·L^{-1})				Ion proportion / wt%			
	SO_4^{2-}	SO_3^{2-}	S^{2-}	$S_2O_3^{2-}$	SO_4^{2-}	SO_3^{2-}	S^{2-}	$S_2O_3^{2-}$
pH = 8	0.042	$<10^{-6}$	0.042	63.159	0.066	$<10^{-5}$	0.066	99.867
pH = 10	0.566	$<10^{-6}$	0.566	62.111	0.895	$<10^{-5}$	0.895	98.210
pH = 12	2.500	$<10^{-6}$	2.500	58.243	3.953	$<10^{-5}$	3.953	92.094

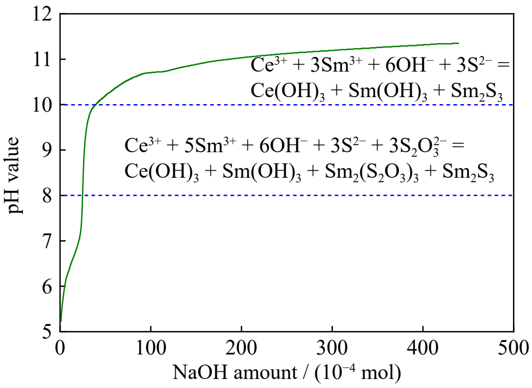

Fig. 1. Titration curve of mixed solutions.

cerium hydroxide generates. In addition, there was also a part of samarium sulfide in the precipitation.

The result of EA of samples is summarized in Fig. 2, which shows that with the increase in pH, the contents of cerium (Ce), samarium (Sm), and oxygen (O) show an upward trend, whereas that of sulfur (S) exhibits a downward trend. What's more, the molar ratio of Sm and Ce in the samples is roughly consistent with the added amount (The molar ratio of Sm and Ce is 3/1).

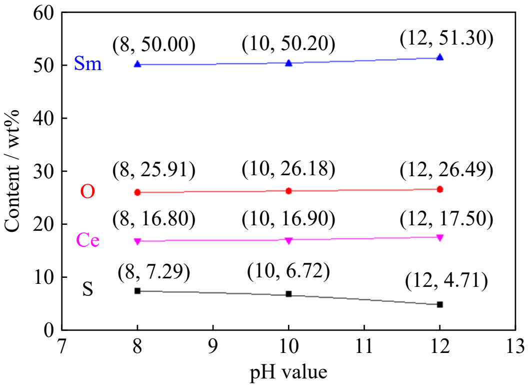

Fig. 2. Element content of samples.

Fig. 3 is the XRD patterns of the three groups of precursors. It can be seen from the Fig. 3 that the precursors have no good crystal morphology. Fig. 4 presents XRD patterns of samples. The samples contained phase Ce_4O_7, Sm_2O_2S, Sm_2O_3, or $Sm_2O_2SO_4$ (When pH value is 12, the diffraction peaks of $Sm_2O_2SO_4$ is not obvious or even disappeared). Combined with the above results, the reaction equations during roasting process are speculated to include Eqs. (2)–(5).

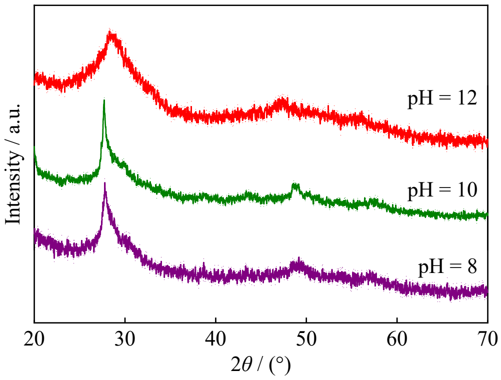

Fig. 3. XRD patterns of precursors.

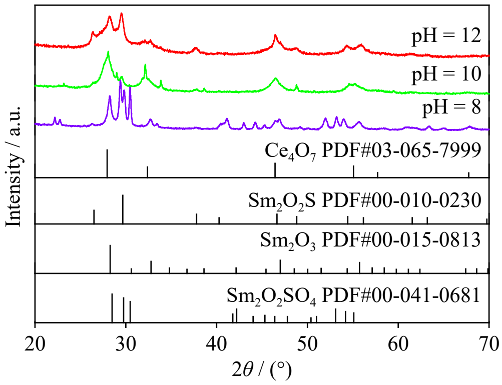

Fig. 4. XRD patterns of samples.

$$4Ce(OH)_3 = Ce_4O_7 + 5H_2O + H_2 \tag{2}$$

$$2Sm(OH)_3 = Sm_2O_3 + 3H_2O \tag{3}$$

$$Sm_2(S_2O_3)_3 + 5H_2O = Sm_2O_2SO_4 + 5H_2S + 4O_2 \tag{4}$$

$$Sm_2S_3 + 2H_2O = Sm_2O_2S + 2H_2S \tag{5}$$

In order to confirm the presence of these phases in the samples, FTIR and Raman characterizations were also performed. Fig. 5 shows the FTIR spectra of the samples. When pH value is 8 and 10, there is a similar FTIR spectrum. The broad band centered at 1191 (1195) and 1052 (1058) cm^{-1} are derived from SO_4^{2-} that confirmed samarium oxysulfate is formed. The band located at 1105 (1109) and 995 (996) cm^{-1} is attributable to O_2S^{6-}. The absorption bands at 660 and 620 cm^{-1} are the characteristic bending modes of RE–O and RE–S, respectively. As pH value is 12, there is no characteristic peak of SO_4^{2-}, which is consistent with the results of XRD.

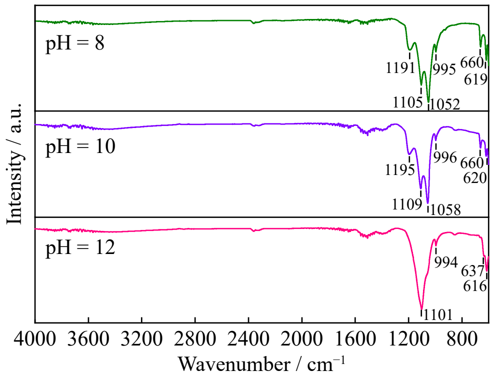

Fig. 5. FTIR spectra of roasted samples.

For purpose of proving that the binding ability of cerium and sulfur is weaker than samarium and sulfur, we prepared the single-system compounds cerium oxysulfide (SOC) and samarium oxysulfide (SOS) respectively, and conducted Raman spectra of the roasted samples, as shown in Fig. 6. Fig. 6(a) shows the Raman spectra of SOC. The band at 457 cm^{-1} should be assigned to F_{2g} mode in cubic fluorite structure. The band at 579 and 1172 cm^{-1} can be attributed to oxygen vacancy. The band at 1021 cm^{-1} corresponds to the signal

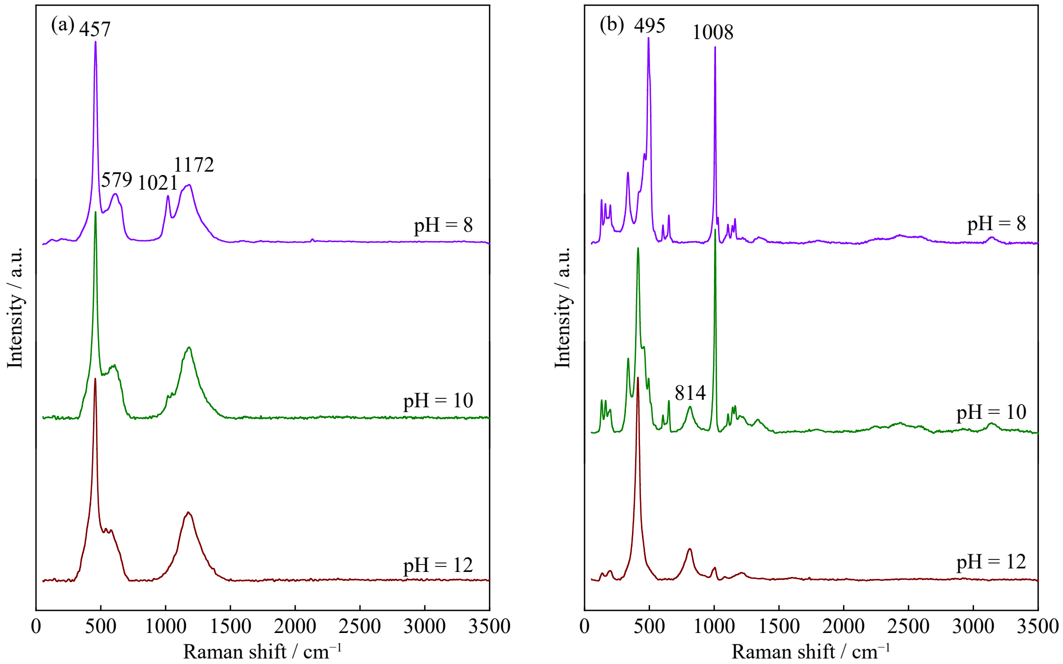

Fig. 6. Raman spectra of (a) SOC and (b) SOS.

peak of adsorbed O^{2-} on the surface, which also indicates the existence of oxygen vacancy. Fig. 6(b) presents the Raman spectra of SOS. The Raman peaks at 1008, 814, and 495 cm^{-1} belong to $Sm_2O_2(SO_4)_3$, Sm_2O_2S, and Sm_2O_3, reapectively.

Fig. 7 shows the SEM images of the precursors prepared under different pH values. The particle size shows a decreasing trend, and the dispersion also gradually get better. Analysis of roasted samples by SEM (Fig. 8) reveal that particle size decreased with the increase in pH. The pH value changed from 8 to 12, and the morphology of samples changes from lamellar to spherical. Fig. 9 shows TEM images and the corresponding selected area electron diffraction (SAED) patterns. As indicated in Fig. 9, the roasted samples are made up of Sm_2O_2S, Sm_2O_3, Ce_4O_7, or $Sm_2O_2SO_4$. In addition, the morphology of TEM is consistent with that of SEM.

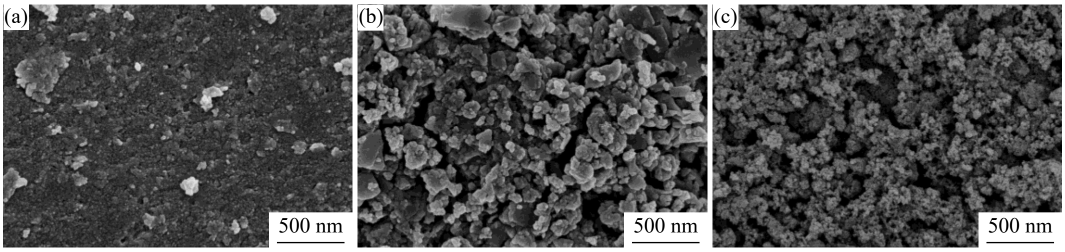

Fig. 7. SEM images of precursors from different pH solutions: (a) pH = 8; (b) pH = 10; (c) pH = 12.

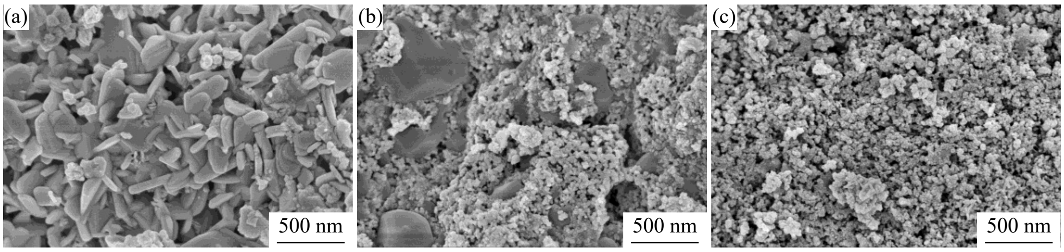

Fig. 8. SEM images of roasted samples from different pH solutions: (a) pH = 8; (b) pH = 10; (c) pH = 12.

Fig. 10 shows the XPS spectra of Ce 3d and O 1s obtained from as-prepared samples. As presented in Fig. 10(a), cerium possesses two valence states, namely, Ce^{3+} and Ce^{4+}. The peaks v and v_0 at 903.9 and 884.3 eV, respectively, belong to Ce^{3+}, whereas the other peaks belong to Ce^{4+}. Oxygen has two valence states, oxygen vacancy (OV) and lattice oxygen (O_β), corresponding to 531.7 and 529.0 eV, respectively [46]. The percentages of Ce^{3+}, Ce^{4+}, Ce^{3+}/Ce^{4+}, OV, O_β, and OV/O_β were calculated based on the XPS spectra of Ce 3d and O 1s (Table 2). As shown in Table 2, the percentage of Ce^{3+} and OV decreases with the increase in pH, whereas that of Ce^{4+} and O_β increases.

Fig. 11 shows UV–Vis transmittance and $(\alpha h\nu)^2$ varies with $h\nu$ curves of all samples in the experiment. Compared

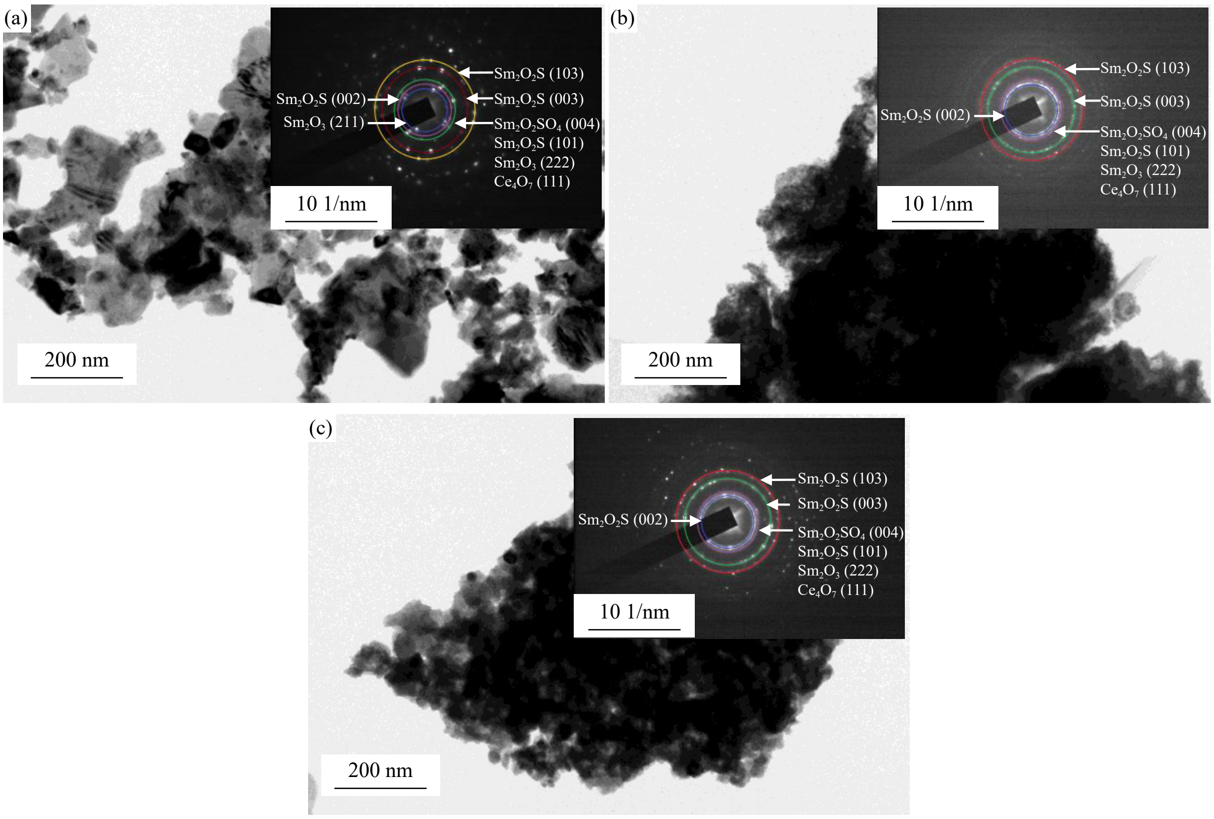

Fig. 9. TEM images and corresponding SAED patterns of roasted samples from different pH solutions: (a) pH = 8; (b) pH = 10; (c) pH = 12.

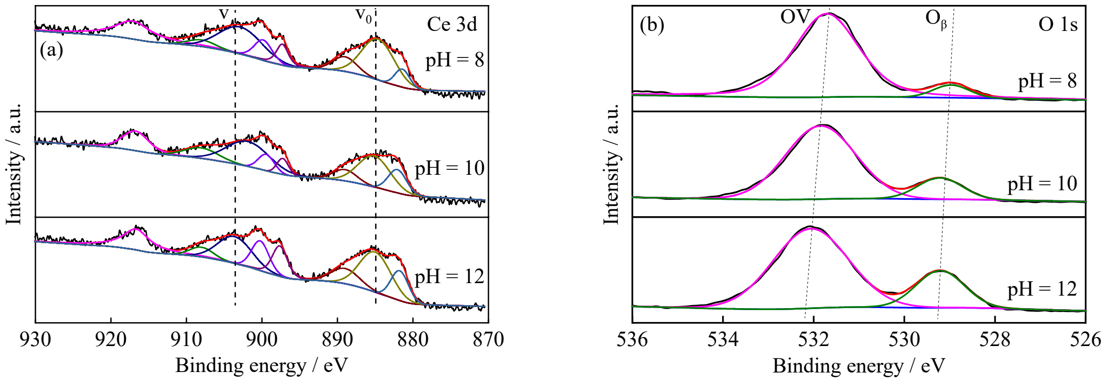

Fig. 10. XPS spectra of (a) Ce 3d and (b) O 1s for the roasted samples.

Table 2. Surface element contents of roasted samples

Sample	Ce^{3+} / mol%	Ce^{4+} / mol%	Ce^{3+}/Ce^{4+}	OV / mol%	O_β / mol%	OV/O_β
pH = 8	49.81	50.19	0.99	93.26	6.74	13.84
pH = 10	49.77	50.23	0.99	84.41	15.59	5.41
pH = 12	41.17	58.83	0.70	77.29	22.71	3.40

with CeO_2 in our previous study [15], the samarium–cerium compounds prepared in this experiment show good shielding effect in ultraviolet and visible light regions. The values of average transmittance between 360 and 450 nm were calculated based on UV–Vis transmittance curves to compare the UV–Vis shielding performance of the samples intuitively (Table 3). As shown in Table 3, average transmittance (360–450 nm) shows a decreasing trend with the increase in pH. As pH value is 12, the minimum value of average transmittance is 8.90%. The band gap was also calculated according to the UV–Vis transmittance curves (Table 3), the minimum value of which is only 2.76 eV. Both the average transmittance and the band gap of the compounds are better than that of CeO_2.

Based on the previous characterization, there are three reasons for the decrease of band gap of the samarium–cerium compound. Firstly, the doping of Sm^{3+} and Ce^{3+} causes a lot of oxygen vacancies in the sample. The oxygen vacancies

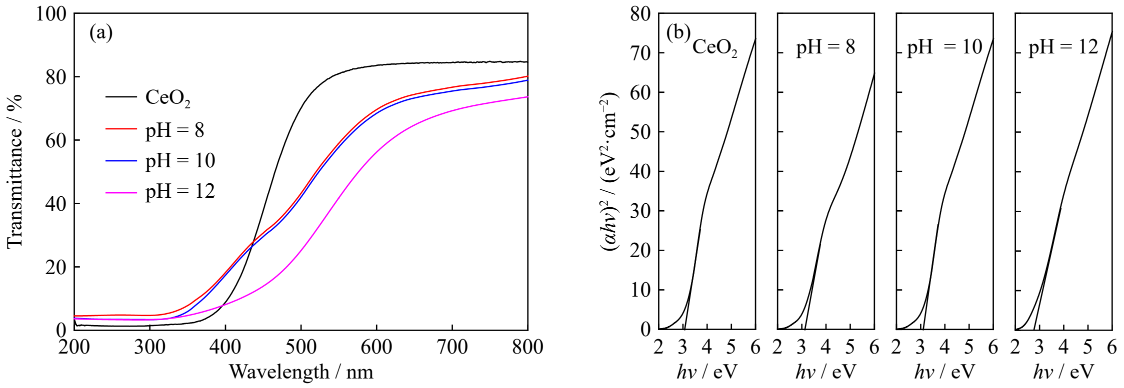

Fig. 11. Ultraviolet–visible transmittance (a) and $(\alpha h\nu)^2$ varies with $h\nu$ (b) curves.

Table 3. Average transmittance and band gap of samples

Sample	Transmittance (360–450 nm) / %	Band gap / eV
CeO$_2$	13.96	3.01
pH = 8	19.77	3.09
pH = 10	18.69	3.08
pH = 12	8.90	2.76

will cause the impurity energy level to appear below the conduction band, thus reducing the band gap, as shown in Fig. 12. Secondly, the ionic radii of Sm^{3+} (0.0958 nm) and Ce^{3+} (0.102 nm) are larger than that of Ce^{4+} (0.087 nm), so there will be a certain degree of lattice expansion, which will also reduce the band gap. Finally, Sm$_2$O$_2$S itself is a good light absorbing material.

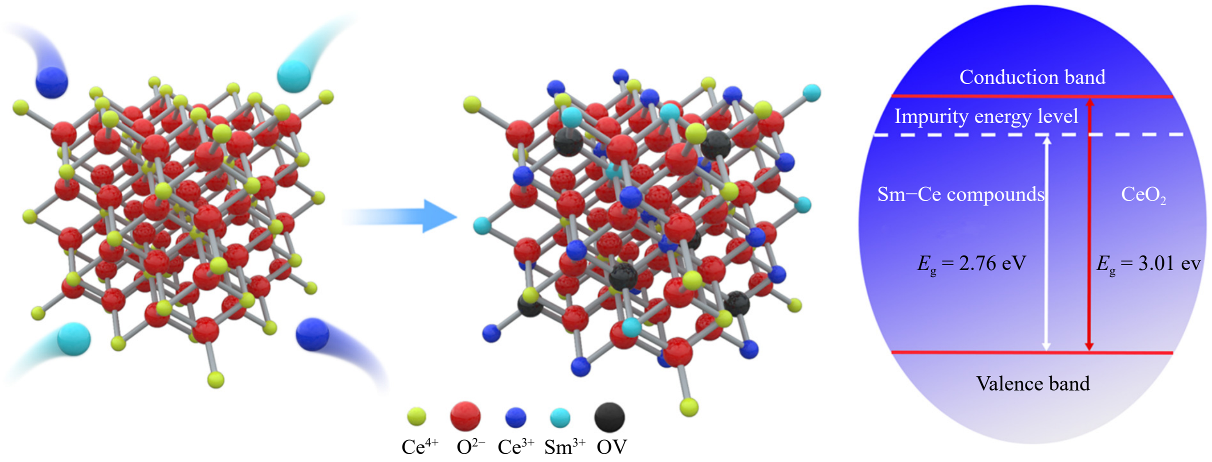

Fig. 12. Mechanism diagram of change in band gap.

4. Conclusion

Co-precipitation method was used to synthesize samarium–cerium compounds containing Sm$_2$O$_2$S. EA indicated that the sulfur content in the compound was negatively correlated with the pH. XRD, FTIR, and Raman spectra showed the samples contained Sm$_2$O$_2$S, Sm$_2$O$_3$, Ce$_4$O$_7$, or Sm$_2$O$_2$SO$_4$. The morphology changed from lamellar to spherical with the increase in pH according to SEM and TEM images. Cerium had two valence states of Ce^{3+} and Ce^{4+}, and oxygen had two forms of OV and O$_\beta$. With the increase in pH, the contents of Ce^{3+} and OV decreased, whereas that of Ce^{4+} and O$_\beta$ increased. Average transmittance (360–450 nm) and band gap were determined by UV–Vis transmittance curve. Among all samples, the minimum average transmittance (360–450 nm) reached 8.90% as pH value was 12, and the minimum band gap was only 2.76 eV, much smaller than that of cerium oxide (3.01 eV). Therefore, the prepared samarium–cerium compounds block not only UV light, but also blue light, which is part of visible light.

Acknowledgements

This work was financially supported by the Major State Basic Research Development Program of China (973 Program) (No. 2012CBA01205) and the National Natural Science Foundation of China (No. 51274060).

Conflict of Interest

The authors declare no conflict of interest.

References

[1] M. Montazer, E. Pakdel, and M.B. Moghadam, Nano titanium dioxide on wool keratin as UV absorber stabilized by butane tetra carboxylic acid (BTCA): A statistical prospect, *Fibers Polym.*, 11(2010), No. 7, p. 967.

[2] K. Lim, W.S. Chow, and S.Y. Pung, Enhancement of thermal stability and UV resistance of halloysite nanotubes using zinc oxide functionalization via a solvent-free approach, *Int. J. Miner. Metall. Mater.*, 26(2019), No. 6, p. 787.

[3] S. Gangopadhyay, D.D. Frolov, A.E. Masunov, and S. Seal, Structure and properties of cerium oxides in bulk and nanoparticulate forms, *J. Alloys Compd.*, 584(2014), p. 199.

[4] S.S. Zhang, J. Li, X.P. Guo, L.H. Liu, H. Wei, and Y.W. Zhang, Nanostructured composite films of ceria nanoparticles with anti-UV and scratch protection properties constructed using a layer-by-layer strategy, *Appl. Surf. Sci.*, 382(2016), p. 316.

[5] C.W. Sun, H. Li, H.R. Zhang, Z.X. Wang, and L.Q. Chen, Controlled synthesis of CeO_2 nanorods by a solvothermal method, *Nanotechnology*, 16(2005), No. 9, p. 1454.

[6] T. Pirmohamed, J.M. Dowding, S. Singh, B. Wasserman, E. Heckert, A.S. Karakoti, J.E.S. King, S. Seal, and W.T. Self, Nanoceria exhibit redox state-dependent catalase mimetic activity, *Chem. Commun.*, 46(2010), No. 16, p. 2737.

[7] A.B. Shcherbakov, N.M. Zholobak, V.K. Ivanov, O.S. Ivanova, A.V. Marchevsky, A.E. Baranchikov, N.Y. Spivak, and Y.D. Tretyakov, Synthesis and antioxidant activity of biocompatible maltodextrin-stabilized aqueous sols of nanocrystalline ceria, *Russ. J. Inorg. Chem.*, 57(2012), No. 11, p. 1411.

[8] X.C. Dai, Z.M. Tang, Y.H. Ju, N. Ni, H.Q. Gao, J.J. Wang, L.Q. Yin, A.L. Liu, S.J. Weng, J.H. Zhang, J. Zhang, and P. Gu, Effects of blue light-exposed retinal pigment epithelial cells on the process of ametropia, *Biochem. Biophys. Res. Commun.*, 549(2021), p. 14.

[9] I. Dumitrescu, O.G. Iordache, C.E. Mitran, E. Perdum, I.M. Săndulache, L.O. Secăreanu, L.C. Dincă, A. Sobetkii, and L. Diamandescu, Attempts to improve the self-cleaning effect of the textile materials, *Ind. Textilă*, 71(2020), No. 3, p. 252.

[10] L.N. Chi, Y.J. Qian, J.Q. Guo, X.Z. Wang, H. Arandiyan, and Z. Jiang, Novel g-C_3N_4/TiO_2/PAA/PTFE ultrafiltration membrane enabling enhanced antifouling and exceptional visible-light photocatalytic self-cleaning, *Catal. Today*, 335(2019), p. 527.

[11] K.S. Su, Y.Y. Tao, and J. Zhang, Highly transparent plasticized PVC composite film with ideal ultraviolet/high-energy short-wavelength blue light shielding, *J. Mater. Sci.*, 56(2021), No. 30, p. 17353.

[12] M.R. Hamblin, Fullerenes as photosensitizers in photodynamic therapy: Pros and cons, *Photochem. Photobiol. Sci.*, 17(2018), No. 11, p. 1515.

[13] A.M. Pires, O.A. Serra, and M.R. Davolos, Yttrium oxysulfide nanosized spherical particles doped with Yb and Er or Yb and Tm: Efficient materials for up-converting phosphor technology field, *J. Alloys Compd.*, 374(2004), No. 1-2, p. 181.

[14] P.D. Han, X.G. Huang, and Q.T. Zhang, Laser stealth absorbent of samarium oxysulfide prepared by flux method, *Rare Met.*, 30(2011), No. 6, p. 616.

[15] Y.P. Li, X. Bian, Y. Liu, W.Y. Wu, and G.F. Fu, Synthesis and characterization of ceria nanoparticles by complex-precipitation route, *Int. J. Miner. Metall. Mater.*, 29(2022), No. 2, p. 292.

[16] E. Matijević and W.P. Hsu, Preparation and properties of monodispersed colloidal particles of lanthanide compounds: I. Gadolinium, europium, terbium, samarium, and cerium(III), *J. Colloid Interface Sci.*, 118(1987), No. 2, p. 506.

[17] A. Verma, N. Karar, A.K. Bakhshi, H. Chander, S.M. Shivaprasad, and S.A. Agnihotry, Structural, morphological and photoluminescence characteristics of sol–gel derived nano phase CeO_2 films deposited using citric acid, *J. Nanopart. Res.*, 9(2007), No. 2, p. 317.

[18] L.X. Yin, Y.Q. Wang, G.S. Pang, Y. Koltypin, and A. Gedanken, Sonochemical synthesis of cerium oxide nanoparticles-effect of additives and quantum size effect, *J. Colloid Interface Sci.*, 246(2002), No. 1, p. 78.

[19] D.S. Zhang, H.X. Fu, L.Y. Shi, C.S. Pan, Q. Li, Y.L. Chu, and W.J. Yu, Synthesis of CeO_2 nanorods via ultrasonication assisted by polyethylene glycol, *Inorg. Chem.*, 46(2007), No. 7, p. 2446.

[20] Y.C. Zhou, R.J. Phillips, and J.A. Switzer, Electrochemical synthesis and sintering of nanocrystalline cerium(IV) oxide powders, *J. Am. Ceram. Soc.*, 78(1995), No. 4, p. 981.

[21] J. Wang, W. Zeng, and Z.C. Wang, Assembly of 2D nanosheets into 3D flower-like NiO: Synthesis and the influence of petal thickness on gas-sensing properties, *Ceram. Int.*, 42(2016), No. 3, p. 4567.

[22] Y. Chen, T.M. Liu, C.L. Chen, W.W. Guo, R. Sun, S.H. Lv, M. Saito, S. Tsukimoto, and Z.C. Wang, Synthesis and characterization of CeO_2 nano-rods, *Ceram. Int.*, 39(2013), No. 6, p. 6607.

[23] Y. Chen, S.H. Lv, C.L. Chen, C.J. Qiu, X.F. Fan, and Z.C. Wang, Controllable synthesis of ceria nanoparticles with uniform reactive {100} exposure planes, *J. Phys. Chem. C*, 118(2014), No. 8, p. 4437.

[24] M.L. Zhang, Y. Chen, C.J. Qiu, X.F. Fan, C.L. Chen, and Z.C. Wang, Synthesis and atomic-scale characterization of CeO_2 nano-octahedrons, *Physica E*, 64(2014), p. 218.

[25] Y. Chen, T.M. Liu, C.L. Chen, W.W. Guo, R. Sun, S.H. Lv, M. Saito, S. Tsukimoto, and Z.C. Wang, Hydrothermal synthesis of ceria hybrid architectures of nano-rods and nano-octahedrons, *Mater. Lett.*, 96(2013), p. 210.

[26] Y. Chen, C.J. Qiu, C.L. Chen, X.F. Fan, S.B. Xu, W.W. Guo, and Z.C. Wang, Facile synthesis of ceria nanospheres by $Ce(OH)CO_3$ precursors, *Mater. Lett.*, 122(2014), p. 90.

[27] P.F. Hu, Y. Chen, R. Sun, Y. Chen, Y.R. Yin, and Z.C. Wang, Synthesis, characterization and frictional wear behavior of ceria hybrid architectures with {111} exposure planes, *Appl. Surf. Sci.*, 401(2017), p. 100.

[28] C.L. Lo, J.G. Duh, B.S. Chiou, C.C. Peng, and L. Ozawa, Synthesis of Eu^{3+}-activated yttrium oxysulfide red phosphor by flux fusion method, *Mater. Chem. Phys.*, 71(2001), No. 2, p. 179.

[29] Y.H. Tseng, B.S. Chiou, C.C. Peng, and L. Ozawa, Spectral properties of Eu^{3+}-activated yttrium oxysulfide red phosphor, *Thin Solid Films*, 330(1998), No. 2, p. 173.

[30] Y.J. Ding, L.X. Wang, Q.T. Zhang, and S.B. Pan, Enhanced luminescence of La^{3+}-doped gadolinium oxysulfide with tunable crystalline size, *J. Electron. Mater.*, 46(2017), No. 10, p. 5986.

[31] B.F. Lei, Y.L. Liu, G.B. Tang, Z.R. Ye, and C.S. Shi, Unusual afterglow properties of Tm^{3+} doped yttrium oxysulfide, *Chem. Res. Chin. Univ.*, 24(2003), No. 5, p. 782.

[32] A. Ishikawa, Y. Yamada, T. Takata, J.N. Kondo, M. Hara, H. Kobayashi, and K. Domen, Novel synthesis and photocatalytic activity of oxysulfide $Sm_2Ti_2S_2O_5$, *Chem. Mater.*, 15(2003), No. 23, p. 4442.

[33] A.N. Georgobiani, A.A. Bogatyreva, V.M. Ishchenko, O.Y. Manashirov, V.B. Gutan, and S.V. Semendyaev, A new multifunctional phosphor based on yttrium oxysulfide, *Inorg. Mater.*, 43(2007), No. 10, p. 1073.

[34] S. Altmannshofer and D. Johrendt, Synthesis, crystal structure and magnetism of the new oxysulfide $Ce_3NbO_4S_3$, *Z. Anorg. Allg. Chem.*, 634(2008), No. 8, p. 1361.

[35] F. Zhao, M. Yuan, W. Zhang, and S. Gao, Monodisperse lanthanide oxysulfide nanocrystals, *J. Am. Chem. Soc.*, 128(2006), No. 36, p. 11758.

[36] R.V. Rodrigues, L.C. Machado, J.R. Matos, E.J.B. Muri, A.A.L. Marins, H.F. Brito, and C.A.C. Passos, Oxysulfate/oxysulfide of Tb^{3+} obtained by thermal decomposition of terbium sulfate hydrates under different atmospheres, *J. Therm. Anal. Calorim.*, 122(2015), No. 2, p. 765.

[37] T. Hirai and T. Orikoshi, Preparation of Gd_2O_3: Yb, Er and Gd_2O_2S: Yb, Er infrared-to-visible conversion phosphor ultrafine particles using an emulsion liquid membrane system, *J. Colloid Interface Sci.*, 269(2004), No. 1, p. 103.

[38] J. Thirumalai, R. Chandramohan, S. Auluck, T. Mahalingam, and S.R. Srikumar, Controlled synthesis, optical and electronic properties of Eu^{3+} doped yttrium oxysulfide (Y_2O_2S) nanostruc-

tures, *J. Colloid Interface Sci.*, 336(2009), No. 2, p. 889.

[39] J.B. Lian, X.D. Sun, J.G. Li, and X.D. Li, Synthesis, characterization and photoluminescence properties of $(Gd_{0.99}, Pr_{0.01})_2O_2S$ sub-microphosphor by homogeneous precipitation method, *Opt. Mater.*, 33(2011), No. 4, p. 596.

[40] J. Cichos, M. Karbowiak, D. Hreniak, and W. Stręk, Synthesis and characterization of monodisperse Eu^{3+} doped gadolinium oxysulfide nanocrystals, *J. Rare Earths*, 34(2016), No. 8, p. 850.

[41] K. Ueda, S. Inoue, S. Hirose, H. Kawazoe, and H. Hosono, Transparent p-type semiconductor: LaCuOS layered oxysulfide, *Appl. Phys. Lett.*, 77(2000), No. 17, p. 2701.

[42] J. Dhanaraj, M. Geethalakshmi, R. Jagannathan, and T.R.N. Kutty, Eu^{3+} doped yttrium oxysulfide nanocrystals–crystallite size and luminescence transition(s), *Chem. Phys. Lett.*, 387(2004), No. 1-3, p. 23.

[43] V.V. Bakovets, T.M. Levashova, I.Y. Filatova, E.A. Maksimovskii, and A.E. Kupcha, Vapor phase growth of nanostructured yttrium oxysulfide films, *Inorg. Mater.*, 44(2008), No. 1, p. 67.

[44] J. Tauc, R. Grigorovici, and A. Vancu, Optical properties and electronic structure of amorphous germanium, *Phys. Status Solidi B*, 15(1966), No. 2, p. 627.

[45] E.A. Davis and N.F. Mott, Conduction in non-crystalline systems V. Conductivity, optical absorption and photoconductivity in amorphous semiconductors, *Philos. Mag.*, 22(1970), No. 179, p. 0903.

[46] B.C. Qiu, C. Wang, N. Zhang, L.J. Cai, Y.J. Xiong, and Y. Chai, CeO_2-induced interfacial Co^{2+} octahedral sites and oxygen vacancies for water oxidation, *ACS Catal.*, 9(2019), No. 7, p. 6484.